



Pt NPs-loaded siloxene nanosheets for hydrogen co-evolutions from Zn-H₂O fuel cells-powered water-splitting



Chang Chen ^{a,b}, Han Tian ^a, Zhengqian Fu ^a, Xiangzhi Cui ^{a,b,c,*}, Fantao Kong ^a, Ge Meng ^{a,b}, Yafeng Chen ^d, Fenggang Qi ^{a,b}, Ziwei Chang ^e, Libo Zhu ^{a,b}, Haitao Huang ^f, Bao Yu Xia ^g, Jianlin Shi ^{a,b,*}

^a State Key Laboratory of High Performance Ceramics and Superfine Microstructure, Shanghai Institute of Ceramics, Chinese Academy of Sciences, Shanghai 200050, PR China

^b Center of Materials Science and Optoelectronics Engineering, University of Chinese Academy of Sciences, Beijing 100049, PR China

^c School of Chemistry and Materials Science, Hangzhou Institute for Advanced Study, University of Chinese Academy of Sciences, Hangzhou 310024, PR China

^d Beijing Advanced Innovation Center for Materials Genome Engineering, Collaborative Innovation Center of Steel Technology, University of Science and Technology Beijing, Beijing 100083, PR China

^e School of Physical Science and Technology, Shanghai Tech University, Shanghai 201210, PR China

^f Department of Applied Physics, Hong Kong Polytechnic University, 11 Yucai Road, Kowloon, Hongkong, China

^g Key Laboratory of Material Chemistry for Energy Conversion and Storage (Ministry of Education), Hubei Key Laboratory of Material Chemistry and Service Failure, School of Chemistry and Chemical Engineering, Wuhan National Laboratory for Optoelectronics, Huazhong University of Science and Technology, 1037 Luoyu Road, Wuhan 430074, PR China

ARTICLE INFO

Keywords:

Siloxene
Hydrophilicity
Electronic interaction
Co-productions
Zn-H₂O cell

ABSTRACT

Siloxene features abundant functional groups and oxygen vacancies, which facilitates the ultrafine platinum nanoparticles loading for catalyzing hydrogen evolution reaction (HER). Herein, a siloxene-p-Pt-2 h composite has been fabricated with an ultralow platinum loading on siloxene (0.56 wt%), which shows greatly enhanced HER activity featuring an ultralow overpotential ($\eta_{10} = 23$ mV). Attractively, the siloxene-p-Pt-2 h has been applied as a HER catalyst in a Zn-H₂O fuel cell, demonstrating a high power density of 157 mW cm⁻² in coupling with the cathode hydrogen evolution. Moreover, a coupled configuration between two Zn-H₂O fuel cells in series and the cell-powered hydroxide electrolyzer achieves the efficient hydrogen co-productions co-catalyzed by the HER catalysts. The excellent HER performance is attributed to the hydrophilic character and the optimal Gibbs free energy via the strong interaction between the siloxene and platinum nanoparticles. This work provides a novel design of self-powered co-productions of hydrogen.

1. Introduction

The exploitation of renewable energy and novel energy storage is urgently demanded currently owing to excessive consumption of fossil fuels, in which clean hydrogen (H₂) energy has been considered as the most appealing alternative [1]. Electrochemical water splitting for hydrogen evolution reaction (HER), and also alkaline-acid Zinc (Zn)-H₂O fuel cells featuring HER at the cathode, have been proposed to be the environmental-friendly hydrolysis technology to obtain pure hydrogen [1–4]. Therefore, searching for highly active catalysts for HER would greatly benefit the clean energy conversion and storage, since both water electrolysis and Zn-H₂O fuel cell are oriented by the HER.

Up to date, precious platinum (Pt) demonstrates the most encouraging HER performance [5], and it is still difficult to find useful non-noble metal catalysts to completely substitute for Pt in acid electrolyte on account of the wide gap between the current progressive Pt-based catalysts and Pt-free catalysts [6,7]. Elevating the Pt utilization efficiency and minimizing the usage of Pt by composition-regulating and size-engineering strategies, etc., are the most effective approaches currently [8–10]. Consequently, the primary challenge and ultimate target are to design cost-effective Pt-based HER electrocatalysts which displays strong intrinsic catalytic activity with ultralow amount of Pt by tailoring their compositions and structures.

Substrates in composite catalysts are expected to offer dispersion,

* Corresponding authors at: State Key Laboratory of High Performance Ceramics and Superfine Microstructure, Shanghai Institute of Ceramics, Chinese Academy of Sciences, Shanghai 200050, China.

E-mail addresses: cuixz@mail.sic.ac.cn (X. Cui), jshi@mail.sic.ac.cn (J. Shi).

protection and synergistic activation functions to boost the HER activities of loaded active species such as Pt, which is prone to severe agglomeration and poor durability without the substrates during electrochemical processes. Up to now, significant progress has been made on hunting for a variety of substrates for Pt, among which, two-dimensional (2D) materials [11–14], have drawn extensive attention to enhance the electrocatalytic performance based on the metal-support interactions [15,16]. Compared with bulk phase materials, 2D materials expose most surface atoms and active sites, hence greatly augmenting the atomic utilization [17]. By tuning the thickness and doping other elements in 2D material, and the introductions of defects such as vacancies, the electronic structure can be regulated leading to the accelerated electron transport and the increased catalytic performance [18].

2D Si-based nanosheets are most likely to be the powerful competitors to other 2D materials benefiting from the larger electronegativity of Pt ($X = 2.28$) than that of Si ($X = 1.98$), which enables the Pt-Si bond formation and the resultant synergistic catalytic effect between the stabilized Pt nanoparticle and the substrate. Especially, siloxene is a type of novel 2D materials in a buckled honeycomb lattice, which is analogous to but essentially different from silicene [19,20]. In contrast to the non-plane structure of silicene with pure Si sp^2 and sp^3 hybridization [21], siloxene nanosheets possess a large amount of dangling bonds, e.g., -O, -OH, etc., on the surface because of the introduction of O species, which offers excellent hydrophilicity favorable for H_2 molecule desorption during water-splitting reaction. On the other hand, the rich functional groups, e.g., -H, -OH, etc. on the surface of siloxene, can be used to effectively anchor the active sites [22,23]. These unique character makes siloxene a potential electrode catalyst in water-splitting and energy storage field [23–27]. Though theoretical calculation for silicene/siloxene anchoring transition metal atoms has been documented [28], however, the application of silicene/siloxene in HER has been rarely reported, and the very few HER activity data available in literatures are far from being desirable mainly because of its very few and unstable surface active sites for metal NPs loading resulting from the harsh synthesis conditions of siloxene, such as ultrahigh vacuum (UHV) deposition using molecular beam epitaxy (MBE) on metallic substrates, etc [21].

In this work, we report the successful synthesis of vacancy-rich 2D siloxene nanosheets possessing abundant surface functional groups facilely by a mild wet-chemical exfoliation method, on which highly dispersive and ultra-small Pt nanoparticles (~ 2 nm) have been photo-deposited by making use of Si-H groups and oxygen vacancies on/in the nanosheets. The obtained siloxene-p-Pt-2 h catalyst displays excellent HER electrocatalytic performances in water splitting, featuring an overpotential of 23 mV at 10 mA cm^{-2} and a Tafel slop of 25.7 mV dec^{-1} , which outperforms the silicene-p-Pt-2 h by using silicene as substrate under the same condition, and the corresponding mass activity is around 38 times of that of commercial Pt/C in acidic electrolyte.

More attractively, Zn-H₂O fuel cell is also an electric power supply device in addition to the self-driven HER, which is thought to be capable of driving the water-splitting for HER without the external energy input, achieving the self-powered H_2 co-productions from both cathodes of the fuel cells and the coupled hydrolyzer for water-splitting. To this end, the siloxene-p-Pt-2 h has also been used as the cathode catalyst in the Zn-H₂O cells for both cathodic HER and power output to drive the water splitting, in which an extremely high power density of 157 mW cm^{-2} was obtained in addition to the excellent stable H_2 production. Greatly encouragingly, a coupled configuration between two Zn-H₂O cells in series and a hydrolyzer has been established to realize the self-powered co-productions of hydrogen from both the fuel cells and electrocatalytic water splitting. Further, the excellent HER performance of siloxene-p-Pt-2 h with as low as 0.56 wt% Pt is attributed to the presences of Si-H groups and oxygen vacancies serving as the anchoring sites to prevent the Pt NPs from aggregating, and on the other hand the formed Pt-Si bonds from the strong interaction between siloxene and Pt NPs modulating the surface electronic structure of Pt, consequently boosting the

HER electrocatalytic activity.

2. Experimental section

2.1. Materials

Calcium silicide (CaSi₂, 95%) was purchased from Sigma-aldrich Chemicals. Hydrochloric acid (HCl) and ethylene glycol were obtained from Sinopharm Chemical Reagent Co., Ltd. Chloroplatinic acid hexahydrate ($H_2PtCl_6 \cdot 6H_2O$, 99.9%), anhydrous acetonitrile (CH_3CN , 99.9%), iodine (I_2 , 99%), and N-Methylpyrrolidone (C_5H_9NO , 99.5%) were purchased from Adamas reagent Co., Ltd. Nafion D-520 dispersion (5 wt%) was purchased from Dupont China Holding Co., Ltd. Commercial 20 wt% Pt/C was obtained from Shanghai HEPHAS Energy Equipment Co., Ltd. All reagents were used as received without further purification.

2.2. Synthesis of silicene nanosheets

Silicene nanosheets were prepared through a facile wet-chemical method. Briefly, a certain amount of precursor CaSi₂ and I₂ powder (molar ratio = 1:1) were added into CH_3CN (150 mL). Subsequently, the mixture was continually stirred at room temperature for 14 days under N₂ atmosphere protection. After completion of the reaction process, the product was centrifuged and washed with anhydrous acetonitrile for several times. Then the obtained product was dispersed in NMP (50 mL) for ultrasonic treatment followed with centrifugation for three times and freeze-drying for overnight.

2.3. Synthesis of siloxene nanosheets

Siloxene nanosheets were synthesized via a facile wet-chemical method. In brief, concentrated HCl (100 mL) was placed in -20 °C condition for 30 min, and then CaSi₂ powder (1 g) was put into concentrated HCl solution under stirring at -20 °C for 7 days. The color of reaction mixture gradually changed from black to green. Subsequently, multilayer siloxene was separated via repeated centrifugation (rpm of 13,000) with deionized water and ethanol. Then the obtained product was dispersed in water (50 mL) followed by ultrasound irradiation. The green siloxene was obtained via centrifugation and freeze-drying for overnight.

2.4. Synthesis of silicene-p-Pt and siloxene-p-Pt

Silicene-p-Pt was prepared by the *in situ* photo-deposition method. Briefly, ethylene glycol (40 mL) was poured into 80 mL reagent bottle named solution A. Silicene nanosheets (30 mg) were dispersed into solution A followed with ultrasound and stirring for 30 min. $H_2PtCl_6 \cdot xH_2O$ (200 μ L, 25 mg mL^{-1}) was dripped into the above solution. The obtained mixed solution was dripped NaOH solution (5 mL, 0.01 M) and stirred for 10 min. Subsequently, the obtained solution was subjected to illumination irradiation by Xe lamp under stirring for 2 h, and then washed with deionized water and ethanol, and freeze-dried for overnight. Siloxene-p-Pt was fabricated through the same method, the only difference being that silicene was replaced with siloxene. By varying the interval of illumination time, we synthesized siloxene-p-Pt-1 h, siloxene-p-Pt-2 h and siloxene-p-Pt-3 h.

2.5. Materials characterization

The Rigaku D/Max-2550 V X-ray diffractometer equipped with a 1.6 kW Cu K α source at a sweep rate of 4° min^{-1} was applied to obtain the XRD patterns. The Nicolet iS10 FTIR spectrometer was operated to acquire FTIR spectra through the KBr technique. Raman spectrum was recorded on a LABRAM HR Evolution with an excitation wavelength of 532 nm. Atomic Force Microscopy (AFM) measurements were

characterized by NT-MDT NTEGRA. X-ray photoelectron spectroscopy (XPS) tests were performed with Thermo Fisher Scientific ESCA Lab 250 and Thermo Scientific K-Alpha+ equipped with monochromatic Al $K\alpha$ radiation. The Hitachi S-4800 and Magellan 400 field emission scanning electron microscopies were applied to collect scanning electron microscope (SEM) images from synthesized samples. Transmission electron microscopy (TEM) patterns were carried out by Tecnai G2 F20 and JEM-2100 F field emission transmission electron microscopies at an acceleration voltage of 120 kV and 200 kV, respectively. The composition and concentration of catalyst were determined by an inductively coupled plasma Optical emission spectroscopy (ICP-OES, Agilent 725). Electron spin resonance (ESR) signals were characterized on a Bruker A300 ESR instrument.

The electrochemical measurements, the details of DFT calculation and the assembly procedure of Zn-H₂O fuel cells can be seen in the [Supporting Information](#).

3. Results and discussion

3.1. Catalyst synthesis and characterization

The wet-chemical synthetic procedure of siloxene-p-Pt catalysts is schemed in [Fig. 1a](#). In brief, the siloxene nanosheets were obtained via wet-chemical exfoliation of bulked CaSi₂ to remove the Ca²⁺ interlayers, and meanwhile the obtained nanosheets were simultaneously functionalized with abundant functional groups of Si-H and Si-OH by using concentrated HCl [24,29]. Then the oxygen vacancies were introduced into siloxene nanosheets after being treated by mechanical exfoliation and illumination [30]. Subsequently, the siloxene-p-Pt catalyst has been synthesized via an *in situ* photo-deposition method, in which the Si-H groups and oxygen vacancies serve as the anchoring sites to prevent

the aggregation of Pt NPs and guarantee their high dispersion. From [Fig. S1](#), siloxene nanosheets as well as the reference sample, silicene nanosheets, have been successfully synthesized, which is significantly different from precursors CaSi₂. The TEM images reveal that both siloxene and silicene nanosheets are thin and almost transparent ([Figs. 1b, S2a](#)), and siloxene (~1.7 nm) is much thinner than silicene (~7 nm) according to the AFM images ([Figs. S2b,d](#)), which exhibits an amorphous structure from the selected area electron diffraction (SAED) in the inset of [Fig. 1b](#). Moreover, the nanosheet morphology of siloxene is still retained after Pt NPs loaded via photo-deposition ([Fig. 1c](#)). As shown in high-angle annular dark-field scanning TEM (HAADF-STEM) patterns ([Fig. 1d](#)) and the EDS mapping ([Fig. 1e](#)), the loaded Pt NPs with size of ~2 nm are dispersed homogeneously on the siloxene support.

3.2. Comparison of silicene-based and siloxene-based catalysts

Compared with silicene, the XRD pattern of siloxene shows a characteristic diffraction peak of SiO₂ at around 24° ([Fig. 2a](#)), and the diffraction peaks at around 28.4° and 47.3° are indexed to the (111) and (220) reflections of crystalline Si (PDF#27-1402), respectively [31]. No CaSi₂ diffraction peak is found in the XRD patterns of both silicene and siloxene, indicating the completely formation of nanosheets. The highly broadened peaks also indicate that the siloxene nanosheets are either nanosized or amorphous [32]. From the Raman spectroscopy spectra ([Fig. 2b](#)), siloxene displays a sharp band at 509 cm⁻¹ and a relatively weak peak at 369 cm⁻¹, attributing to the symmetric stretching (E_{2g}) modes of the Si-Si bonds and Si-Si vibrancy, respectively, which confirms the presence of Si-Si bonds in the planar Si₆ rings. Meanwhile, a new vibrational peak at 485 cm⁻¹ is clear, being attributed to the vibration of Si-O bond [19]. In contrast, silicene only shows two peaks at 384 and 520 cm⁻¹ belonging to the Si-Si bonds without the

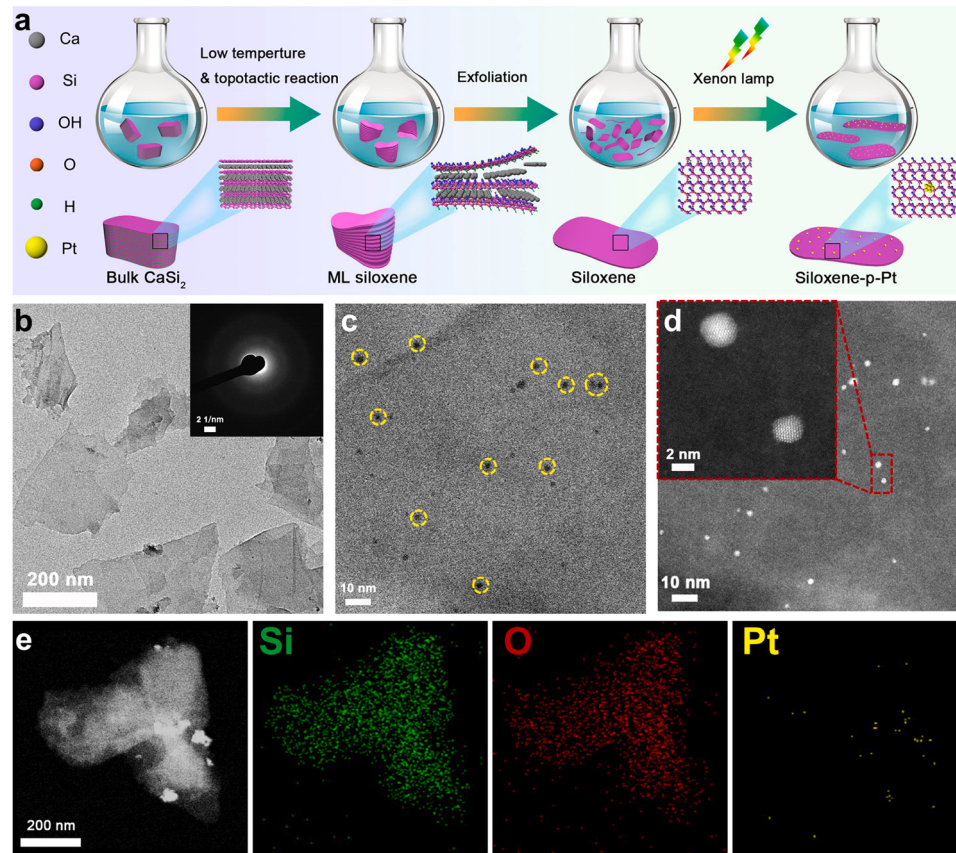


Fig. 1. (a) Schematic illustration of the wet-chemical fabrication of siloxene-p-Pt. (b) TEM images of siloxene with the corresponding SAED images in the insets. (c) TEM, (d) HAADF-STEM images and (e) the corresponding EDX mapping of siloxene-p-Pt-2h.

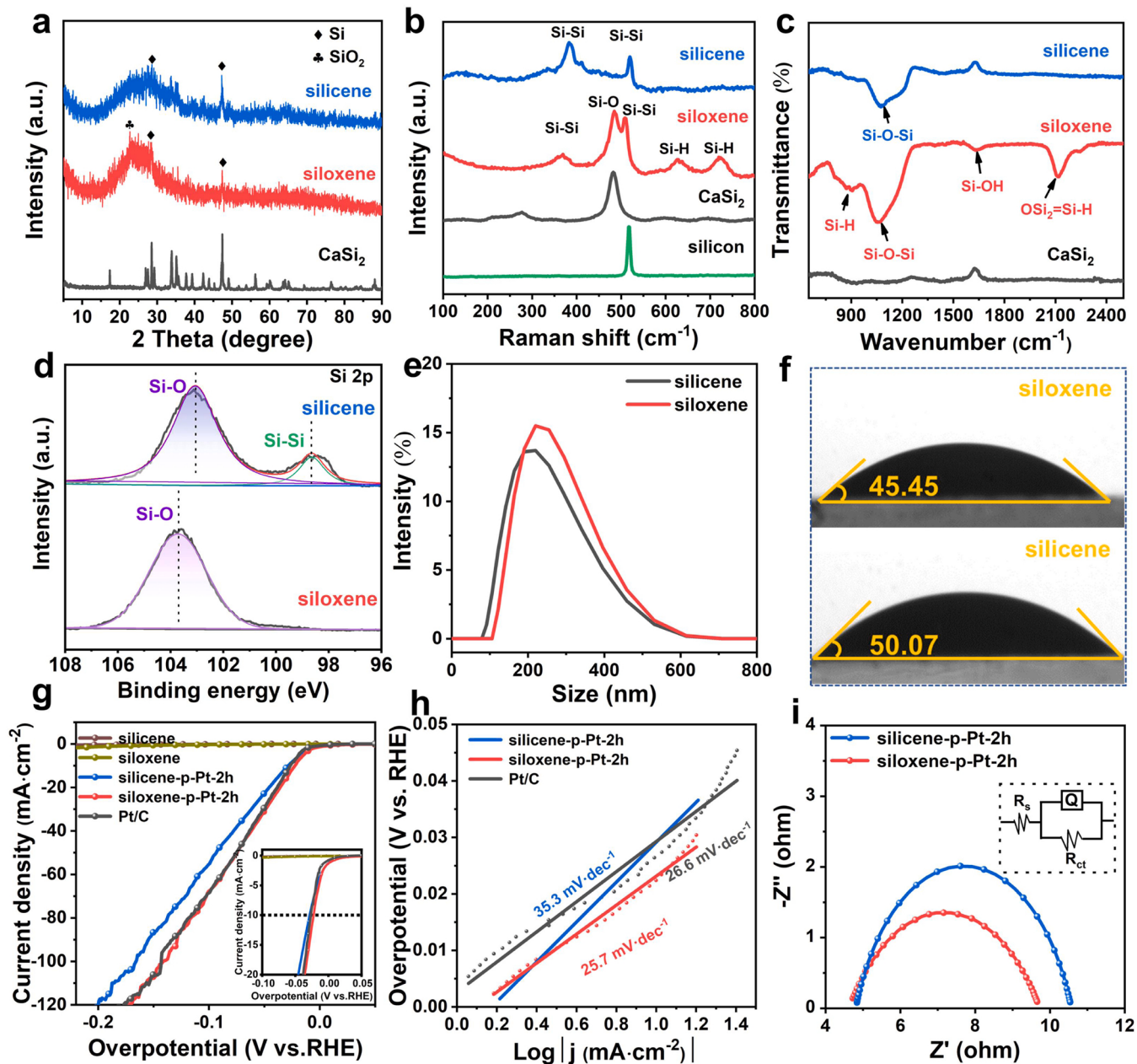


Fig. 2. (a) XRD patterns, (b) Raman spectra, and (c) FTIR spectra of samples. (d) High-resolution Si 2p XPS spectra, (e) Particle-size distribution, and (f) Water contact angle measurements of silicene and siloxene. (g) LSV curves of the prepared samples and 20% Pt/C in 0.5 M H₂SO₄. (h) Tafel plots derived from the corresponding polarization curves. (i) EIS curves of corresponding catalysts with the resistance fitting model in the inset.

characteristic vibrations of Si-O and Si-H bonds, which is different from the pure silicon powder (Fig. 2b). It has been reported that, with the decreases of the thickness of the nanosheets, the full width at half-maximum of the Si-Si (E_{2g}) will be widened and shift to the low frequency (blue shift) [33], confirming that the thickness of siloxene is smaller than that of silicene from the Raman spectroscopic result of siloxene with blue shift. Furthermore, siloxene shows the two broadened peaks at 630 and 723 cm⁻¹, showing the presence of Si-H bonds in consistence with the Raman spectra [24].

The types of the functional groups were further examined using FT-IR spectroscopy (Fig. 2c). Silicene and siloxene demonstrate broadened but distinct bands in comparison to those of bulk CaSi₂. Moreover, siloxene shows the presence of sharp or broad vibration bands at 871, 1061, 1631, and 2118 cm⁻¹ respectively corresponding to the vibrations of $\nu(\text{Si-H})$, $\nu(\text{Si-O-Si})$, $\nu(\text{Si-OH})$, and $\nu(\text{OSi}_2=\text{Si-H})$ [34], further proving

the existence of abundant Si-H and Si-OH groups. For silicene, the band observed at 1070 cm⁻¹ belongs to the vibration of $\nu(\text{Si-O-Si})$, indicating the partially oxidized silicene nanosheets. From the XPS analysis shown in Fig. 2d, the Si 2p peak of siloxene is attributed to Si-O bonding corresponding to the oxygenated and/or hydrated products of silicon [27]. In particular, the Si 2p peak of siloxene shifts toward higher binding energy (103.7 eV), indicating the relatively higher Si valence state in siloxene than in silicene, agreeing well with the O 1s XPS result in Fig. S3. The O 1s spectrum of siloxene presents a peak at a higher binding energy of 533.1 eV than that of silicene, verifying the oxygen- and hydroxyl-functionalized form of siloxene [20,27]. The hydrodynamic size of siloxene nanosheets in aqueous water solution is 240.8 nm (Fig. 2e), which is larger than that of silicene (200.9 nm), due to the easier hydration of the former than the latter in water solution. In addition, the water contact angle of siloxene (45.45°) is also smaller

than that of silicene (50.07°) (Fig. 2f), consolidating the better hydrophilicity of siloxene, further indicating that the siloxene can be well infiltrated and accessed by the electrolyte and therefore conducive to the rapid desorption of H_2 bubbles during the HER reaction [35]. After Pt NPs loading by the same photo-assisted reduction method of 2 h

reduction time, the obtained siloxene-p-Pt-2 h composite shows better homogeneous dispersion of Pt NPs than silicene-p-Pt-2 h because of the existence of surface abundant functional groups on siloxene nanosheets, which can be used to anchor Pt species (Fig. S4). Moreover, due to the existence of functional groups, the amount of Pt in siloxene-p-Pt-2 h

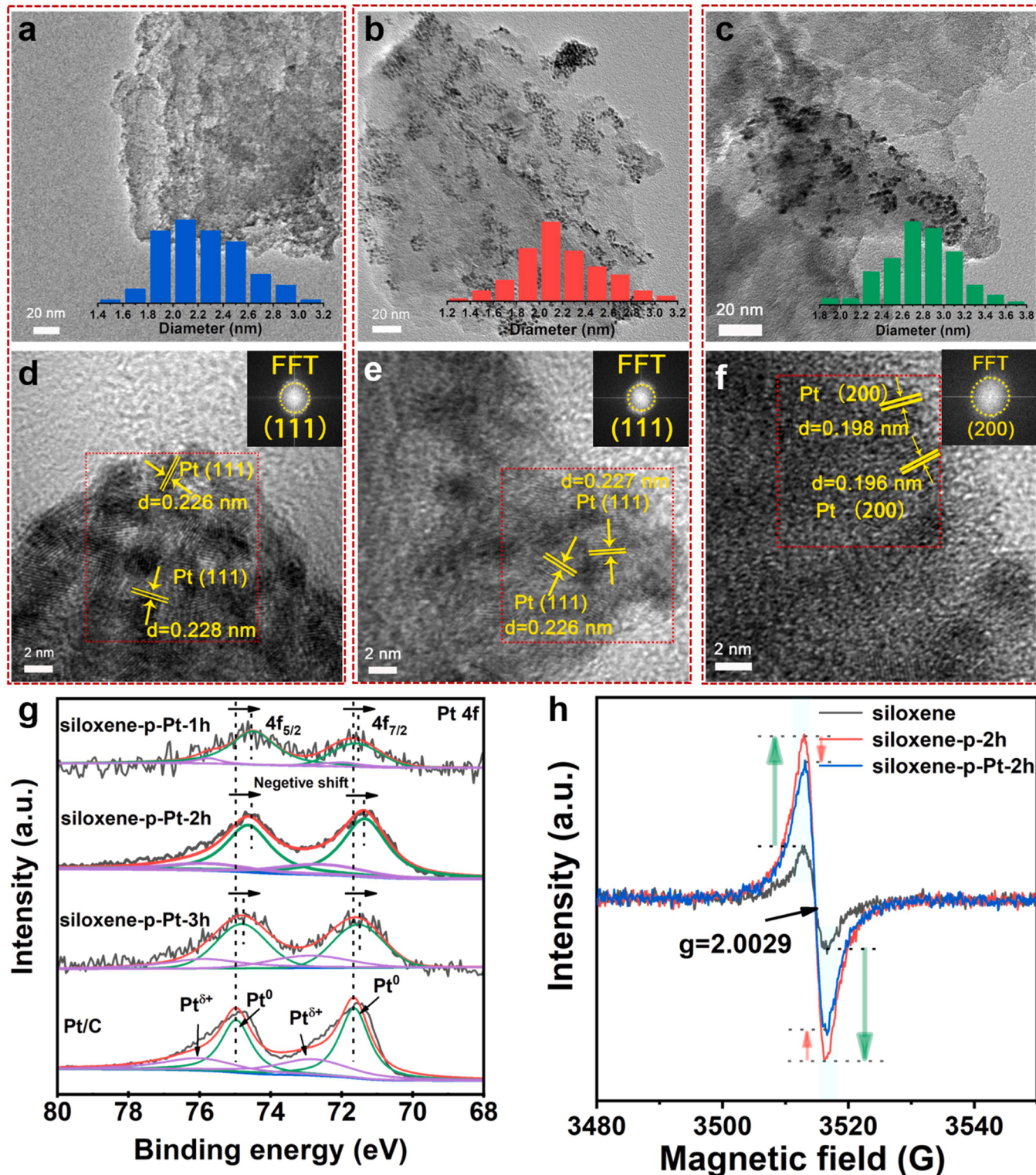


Fig. 3. TEM images of (a) siloxene-p-Pt-1h, (b) siloxene-p-Pt-2h, and (c) siloxene-p-Pt-3h with the corresponding Pt size distribution histograms in the insets. HRTEM images of (d) siloxene-p-Pt-1h, (e) siloxene-p-Pt-2h, and (f) siloxene-p-Pt-3h with the corresponding FFT images in the insets. (g) high-resolution XPS Pt 4f spectra of siloxene-p-Pt samples prepared with different reduction time intervals and commercial Pt/C. (h) ESR spectra of siloxene, siloxene-p-2h and siloxene-p-2h.

composite is slightly higher than that in silicene-p-Pt-2 h according to the ICP-OES in **Table S1**.

As shown in **Fig. 2g**, the pure nanosheets hardly show electrocatalytic performance, indicating that Pt NPs as the dominant active sites play a decisive role in HER. The siloxene-p-Pt-2 h exhibits the highest electrocatalytic activity among the prepared catalysts with an ultralow overpotential of 23 mV at the current density of 10 mA cm^{-2} , which is 5 mV and 4 mV lower than those of silicene-p-Pt-2 h (28 mV) and commercial Pt/C (27 mV), respectively, highlighting the significance of siloxene as the substrate for increasing the HER performance. In addition, the siloxene-p-Pt-2 h shows a Tafel slope of 25.7 mV dec^{-1} , which is much lower than those of silicene-p-Pt-2 h (35.3 mV dec^{-1}) and Pt/C (26.6 mV dec^{-1}), indicating that the HER kinetics on the siloxene-p-Pt-2 h electrocatalyst is mainly determined by the Tafel step (**Fig. 2h**). The better HER electrocatalytic performance of the siloxene-p-Pt-2 h should be attributed to its inherent excellent electrical conductivity, which shows a lower charge transfer resistance (R_{ct}) than silicene-p-Pt-2 h and pure nanosheets according to its smaller radius of the electrochemical AC impedance spectrum (EIS) as shown in **Figs. 2i, S5** and **Table S2**, indicating the faster charge transfer and catalytic reaction kinetics of siloxene-p-Pt-2 h and significantly enhanced conductivity after Pt loading [36]. To understand the different electrocatalytic activities for these samples more accurately, the electrochemical active surface areas (ECSA) were assessed by measuring the capacitance (C_{dl}) in non-Faradaic region because it is linearly proportional to ECSA [37, 38]. The processed data of ECSAs without the contribution by the nanosheet substrate and the exchange current density are shown in **Table S3**. As shown in **Fig. S6**, it can be clearly seen that siloxene-p-Pt-2 h gives the largest C_{dl} of 7.83 mF cm^{-2} , corresponding the ECSA of 197 cm^2 , while silicene-p-Pt-2 h shows the smallest C_{dl} of 4.36 mF cm^{-2} , corresponding the ECSA of 109 cm^2 , further confirming that the siloxene should be the suitable substrate because of its enriched surface functional groups as well as the surface defects as discussed in the following.

3.3. Characterization of siloxene-p-Pt catalysts

To further explore the HER performance of siloxene-p-Pt, different illumination time intervals, 1 and 3 h, for the photo-reduction of Pt, were also adopted to obtain siloxene-p-Pt-1 h and siloxene-p-Pt-3 h, respectively. Similar to siloxene-p-Pt-2 h, siloxene-p-Pt-1 h and siloxene-p-Pt-3 h show no characteristic diffraction peak of Pt (**Fig. S7**) due to the extremely low Pt loadings in siloxene-p-Pt, which are 0.43 wt%, 0.56 wt % and 0.71 wt% for siloxene-p-Pt-1 h, siloxene-p-Pt-2 h and siloxene-p-Pt-3 h (**Table S1**), respectively. No changes of the main structure of siloxene can be found after the Pt NPs loading (**Fig. S8**), meaning the reasonable structure stability of siloxene nanosheets.

From the TEM images in **Figs. 3a–c, S9** and EDX spectra in **Fig. S10**, the siloxene-p-Pt composites exhibit unchanged sheet-like morphology after Pt NPs dispersing, and the insets show that the sizes of Pt NPs in both siloxene-p-Pt-1 h and siloxene-p-Pt-2 h are 1.8–2.8 nm, which slightly increases to 2.4–3.2 nm in siloxene-p-Pt-3 h. Clearly, at increased illumination time duration, more Pt ions will be reduced to Pt metal, which is consistent with the results of ICP-OES (**Table S1**). In addition, the Pt aggregation become significant at the illumination time intervals of longer than 2 h (**Figs. 3c and S9i, j**). It can also be found that in the HR-TEM images, the Pt nanoparticles in siloxene-p-Pt-1 h (**Fig. 3d**) and siloxene-p-Pt-2 h (**Fig. 3e**) present one main (111) plane of the Pt lattice, while siloxene-p-Pt-3 h (**Fig. 3f**) shows an additional (200) plane, agreeing well with the corresponding results of the fast Fourier transform (FFT) in the insets, which is consistent with results of SAED in **Fig. S9c, g and k**. Interestingly, the water contact angle of siloxene-p-Pt-2 h is lower than that of pure siloxene and comparable to commercial Pt/C (**Fig. S11**), indicating the improved hydrophilicity by Pt loading, consequently enhancing the electrocatalytic performance during HER process.

XPS and ESR were adopted for further structure characterizations as

shown in **Figs. 3g–h** and **S12**. Compared with pure siloxene nanosheets, the Si 2p XPS spectra of three siloxene-p-Pt samples have shifted negatively, resulting from the loss of partial O and the formation of oxygen vacancies in the process of illumination [39]. Because of the larger electronegativity of Pt ($X = 2.28$) than that of Si ($X = 1.98$) [40], the Pt species in prepared siloxene-p-Pt catalysts would be more easily reduced into metal, which is proved by the Pt 4f XPS results in **Fig. 3g**. The binding energies of Pt $4f_{5/2}$ and Pt $4f_{7/2}$ for the siloxene-p-Pt-2 h samples show the negative shifts by 0.50 and 0.32 eV, respectively, compared with that of commercial Pt/C, indicating the existence of the electronic interaction between Si and Pt due to the formation of Pt-Si bonds, and consequently lowered valence of Pt species and the formation of metallic Pt NPs [40]. Compared with siloxene-p-Pt-1 h, the Pt 4f peaks in siloxene-p-Pt-2 h show stronger negative shift owing to the increased Pt loading. However, when prolonging illumination to 3 h, the resultant Pt NPs become gradually aggregated with each other, resulting in the positive shift of Pt 4f peak in siloxene-p-Pt-3 h. These results indicate that the Pt species will initially bond with Si because of the presence of siloxene, which is believed to be responsible for the excellent dispersion of the resultant Pt NPs, but the aggregation of Pt NPs will take place at certain elevated Pt loading amount.

Meanwhile, the oxygen vacancies have been induced in siloxene substrate during the photo-reduction according to the Si 2p XPS (**Fig. S12**), which would accelerate the HER. The existence of oxygen vacancies was confirmed by ESR result (**Fig. 3h**). Pure siloxene nanosheets possess a small amount of oxygen vacancies by mechanical exfoliation, while the ESR intensity of siloxene-p-2 h increases dramatically during the first 2 h of light irradiation in ethylene glycol without adding chloroplatinic acid, indicating that the illumination by Xenon lamp can produce plentiful oxygen vacancy defects. When chloroplatinic acid was added and subject to the same illumination, the ESR intensity of Pt-loaded siloxene-p-Pt-2 h become lower than that of siloxene-p-2 h to a certain extent, suggesting the partial reduction of the oxygen vacancy amount by Pt NPs loading on siloxene during the Xenon lamp illumination. These results indicate that the Pt NPs as well as the oxygen vacancies can be introduced simultaneously during the photo-reduction, and moreover the Pt species can be effectively anchored by the oxygen vacancies leading to the homogeneous dispersion of resultant Pt NPs after the photo-reduction.

3.4. Electrocatalytic HER performance

As shown in **Fig. 4a**, samples siloxene-p-Pt-1 h, siloxene-p-Pt-2 h and siloxene-p-Pt-3 h respectively need 26 mV, 23 mV and 42 mV to reach the current density of 10 mA cm^{-2} , and siloxene-p-Pt-2 h displays the best HER performance among the three samples in terms of the overpotential and current density. From **Fig. 4b**, the overpotentials of siloxene-p-Pt-2 h ($\eta_{10} = 23 \text{ mV}$, $\eta_{60} = 87 \text{ mV}$) at both 10 and 60 mA cm^{-2} outperform those of 20% Pt/C ($\eta_{10} = 27 \text{ mV}$, $\eta_{60} = 89 \text{ mV}$), revealing its superior HER catalytic activities even at such an ultralow Pt amount (0.56 wt%). Therefore, the specific mass activity (MA) values of siloxene-p-Pt catalysts are much higher than that of Pt/C (**Fig. 4c**), and the MAs of siloxene-p-Pt-1 h, siloxene-p-Pt-2 h, and siloxene-p-Pt-3 h at the overpotential of 50 mV (inset of **Fig. 4c**) respectively reach 18.71 , 18.22 , and $5.85 \text{ mA } \mu\text{g}_{\text{Pt}}^{-1}$, which are 38.98 , 37.96 , and 12.19 times higher than that of 20% Pt/C ($0.48 \text{ mA } \mu\text{g}_{\text{Pt}}^{-1}$), respectively. The excellent HER performance of siloxene-p-Pt-2 h is associated with its ultra-fast catalytic kinetics, featuring the lowest Tafel slope of 25.7 mV dec^{-1} among the prepared samples (**Fig. 4d**), corresponding to a Volmer-Tafel mechanism [41–43]. In addition, the R_{ct} endows siloxene-p-Pt-2 h (5.09Ω) with the fastest charge transfer kinetics (**Fig. 4e** and **Table S2**). Moreover, siloxene-p-Pt-2 h sample gives the largest C_{dl} and ECSA, compared to siloxene-p-Pt-1 h (7.12 mF cm^{-2} , 178 cm^2) and siloxene-p-Pt-3 h (4.95 mF cm^{-2} , 124 cm^2), which is shown in **Fig. S13** and **Table S3**, and the higher turnover frequency (TOF) than Pt/C at varied overpotentials (**Table S4**), indicating an excellent HER catalytic

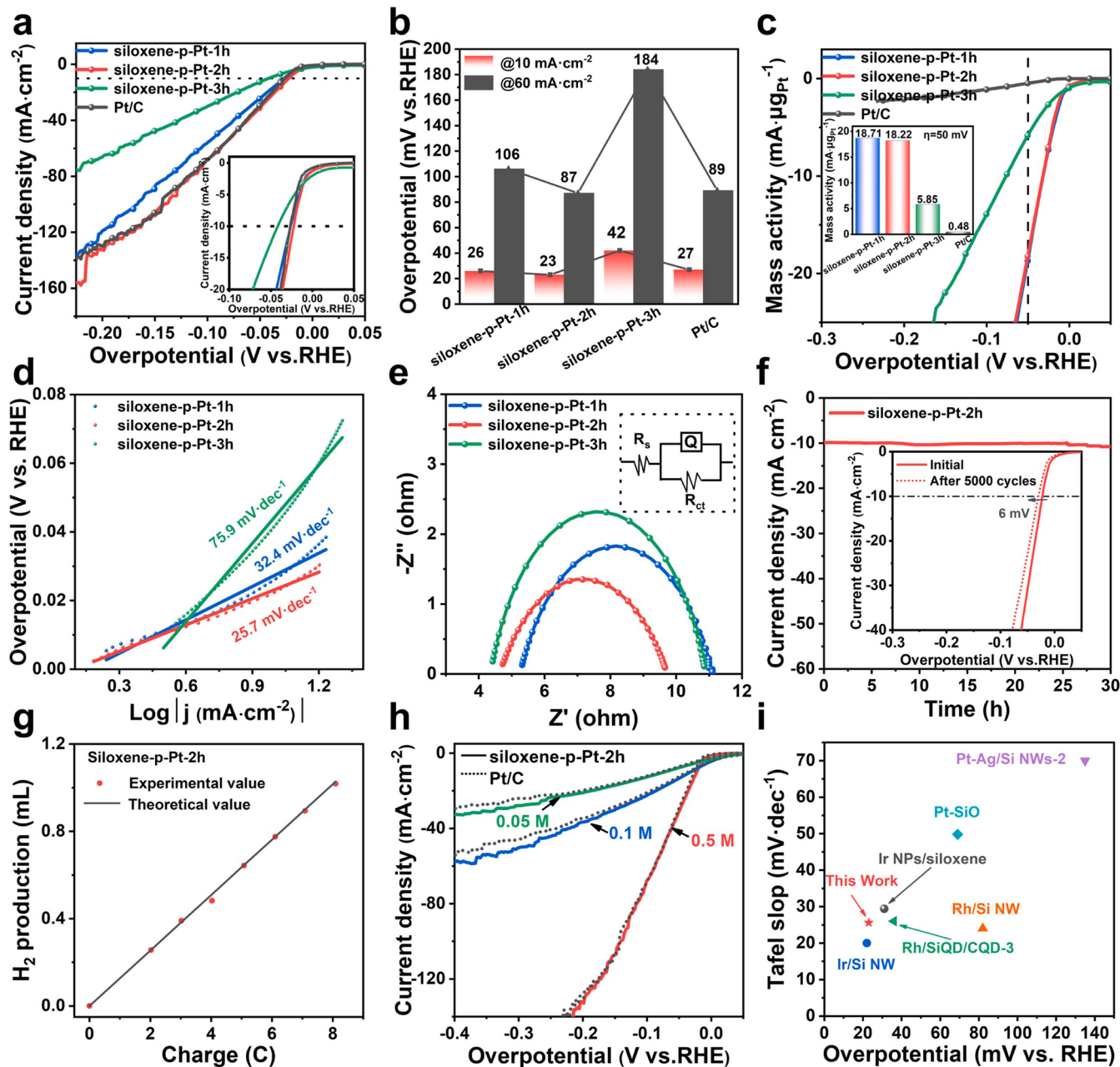


Fig. 4. (a) LSV curves of different catalysts with their low current density region in the inset. (b) Histograms of overpotentials of the catalysts at 10 and 60 mA cm^{-2} . (c) LSV curves normalized to the mass of Pt (inset shows the mass activity histograms at $\eta = 50$ mV). (d) Tafel plots derived from the corresponding polarization curves. (e) EIS curves of corresponding catalysts. (f) Chronopotentiometric curves of siloxene-p-Pt-2 h at 10 mA cm^{-2} (inset: the LSV curves of siloxene-p-Pt-2 h before and after 5000 cycles of scanning). (g) Comparison of experimental H_2 generation volume with theoretical calculation at the overpotential of 23 mV. (h) LSV curves of siloxene-p-Pt-2 h in different concentrations of H_2SO_4 . (i) Comparison of merits with respect to both Tafel slope and overpotential at 10 mA cm^{-2} with references to reported Si-based catalysts in acid media.

activity of siloxene-p-Pt-2 h thanks to the electronic interactions between interfaces of Pt NPs and siloxene substrate.

To assess the durability of siloxene-p-Pt-2 h, accelerated durability tests (ADTs) and i-t chronoamperometry techniques were employed. As shown in the insets of Fig. 4f and Fig. S14, siloxene-p-Pt-2 h displays a potential increase by as low as 6 mV at 10 mA cm^{-2} after 5000 cycles, which is markedly lower than that of Pt/C (21 mV), demonstrating the outstanding cycling stability of siloxene-p-Pt-2 h. After the ADTs, the morphology of siloxene-p-Pt-2 h and the Pt NPs' high dispersion on siloxene remain unchanged (Fig. S15). Compared with the initial sample, the Si 2p XPS of siloxene-p-Pt-2 h after 5000 cycles shifts negatively but slightly (Fig. S16a), and the Pt 4f XPS shifts positively

correspondingly (Fig. S16b), indicating that slight HER performance deterioration is due to the limited weakening of the dominant Pt-Si bonding, i.e., interaction between Pt and Si in the composite catalyst. The excellent electrochemical stability of siloxene-p-Pt-2 h was further confirmed by recording the i-t curves (Fig. 4f), which show no significant attenuation even after 30 h of continuous electrolysis, outperforming Pt/C which shows a sharp decay in the same conditions (Fig. S14). Fig. 4g exhibits the relationship between the charge and the generated H_2 amount, displaying that the measured H_2 amount agrees well with the calculated value, indicating a high Faradic efficiency of 98.4% for H_2 production. To further investigate the HER performance of siloxene-p-Pt-2 h, different concentrations (0.5, 0.1, and 0.05 M) of

H_2SO_4 as the electrolyte were used. As shown in Fig. 4h, the overpotentials of siloxene-p-Pt-2 h at different H_2SO_4 concentrations are comparable and even lower than those of Pt/C, suggesting the excellent HER performance of siloxene-p-Pt-2 h in acidic electrolyte. Encouragingly, the HER performance of the present siloxene-p-Pt-2 h ranks at the top of the Si-based catalysts in terms of overpotential and Tafel slope (Fig. 4i) [23,44–47], even in multitudinous Pt-based catalysts (Table S5).

3.5. $\text{Zn}-\text{H}_2\text{O}$ cell performance

High-purity hydrogen can be electrochemically produced by both conventional electrocatalytic water splitting and metal oxidation fuel

cells, such as alkaline-acid $\text{Zn}-\text{H}_2\text{O}$ fuel cell [2], in which the chemical energy in the zinc metal is converted into the hydrogen produced, and in the meantime, electric power is output. As shown in Fig. 5a, a coupled configuration between two $\text{Zn}-\text{H}_2\text{O}$ cells in series and a hydrolyzer has been established for the self-powered co-productions of hydrogen from both the fuel cells and electrocatalytic water splitting. The double alkaline-acid $\text{Zn}-\text{H}_2\text{O}$ fuel cells in series sever as a chemical energy conversion device for the concurrent HER and electricity generation, to drive the coupled water electrolysis.

To this end, electrochemical performance of single alkaline-acid $\text{Zn}-\text{H}_2\text{O}$ cell by using siloxene-p-Pt-2 h as the cathode catalyst was characterized first by adopting a bipolar membrane to separate the cathode and anode chambers of an alkaline-acid $\text{Zn}-\text{H}_2\text{O}$ cell from each other, in

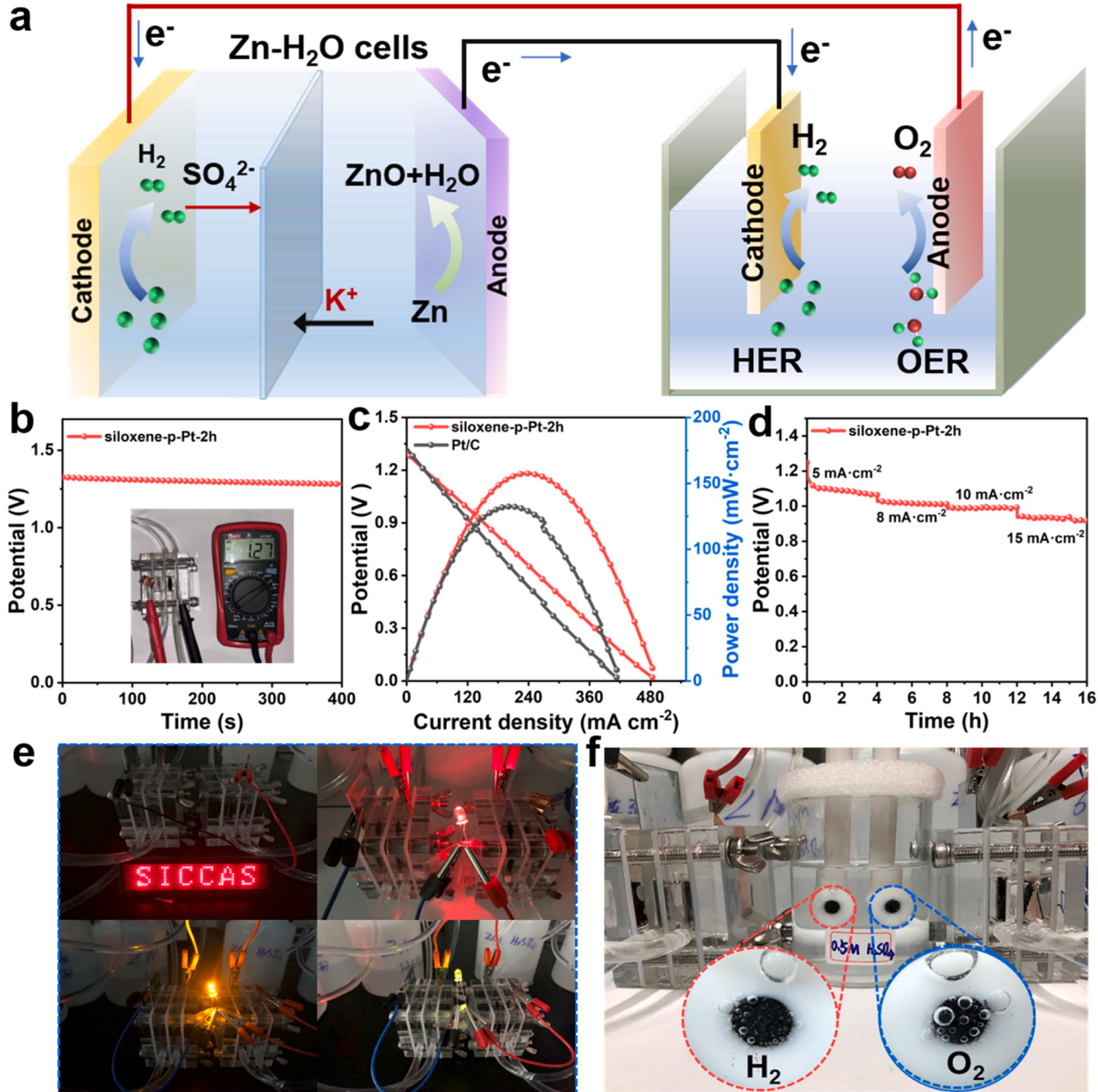


Fig. 5. (a) Schematic illustration of the coupled configuration of double $\text{Zn}-\text{H}_2\text{O}$ cells driving electrocatalytic water splitting. (b) Open-circuit voltage (OCV) plot (inset shows the digital photograph of OCV) for siloxene-p-Pt-2 h equipped $\text{Zn}-\text{H}_2\text{O}$ cell. (c) LSV curves (left-hand y axis) and power density (right-hand y axis) of siloxene-p-Pt-2 h- and Pt/C-equipped $\text{Zn}-\text{H}_2\text{O}$ cell. (d) Chronopotentiometric response at varied current densities of siloxene-p-Pt-2 h-equipped $\text{Zn}-\text{H}_2\text{O}$ cell. (e) Digital photograph of different LED lightened by two siloxene-p-Pt-2 h-based $\text{Zn}-\text{H}_2\text{O}$ fuel cells connected in series. (f) Digital photograph of cathodic HER and anodic OER in the water electrolyzer powered by double $\text{Zn}-\text{H}_2\text{O}$ fuel cells in series (HER catalysts: siloxene-p-Pt-2 h, OER catalysts: RuO₂).

which 2 M H_2SO_4 and 6 M KOH were used as the electrolytes, respectively. The theoretical voltage of Zn- H_2O cell can be as high as 1.33 V [2], benefiting from the chemical thermal energy of acid and alkaline between cathode and anode. The open-circuit voltage (OCV) of the siloxene-p-Pt-2 h-equipied Zn- H_2O cell has been recorded to be around 1.27 V as shown in Fig. 5b, which can be maintained above 1.21 V for 20 h in the long-term OCV tests (Fig. S17), demonstrating the excellent feasibility and stability of the fuel cell device [48,49]. As shown in Fig. 5c, the maximum power density of siloxene-p-Pt-2 h-based Zn- H_2O cell reaches an extraordinarily high value of 157 mW cm^{-2} , which is markedly higher than that of Pt/C-based Zn- H_2O cells (132 mW cm^{-2}). Moreover, the discharge plateau can be maintained stable at varied current densities (Fig. 5d), and the discharge voltages at different current densities of 5, 8, 10 and 15 mA cm^{-2} are 1.07 V, 1.01 V, 0.99 V and 0.91 V, respectively, further indicating high stability of the siloxene-p-Pt-2 h-equipied Zn- H_2O cell.

To demonstrate the potential application of power output from the Zn- H_2O cell device, two siloxene-p-Pt-2 h-equipied Zn- H_2O cells were connected in series and applied to lighten light-emitting diodes (LEDs) as shown in Fig. 5e. Furthermore, a self-powered system was established by coupling two Zn- H_2O cells in series and a hydrolyzer for the co-production of H_2 from both the fuel cells and the fuel cells-driven electrocatalytic water splitting, in which siloxene-p-Pt-2 h was employed as the cathodes in both the fuel cells and the electrochemical hydrolyzer. Such a self-powered system has been operated smoothly for a long time period, as illustrated in Figs. 5f and S18.

3.6. DFT calculation

To further investigate the electrocatalytic mechanism, DFT calculations were carried out to analyze the electrocatalytic thermodynamics and kinetics of pure silicene, pure siloxene and siloxene-p-Pt. Fig. S19

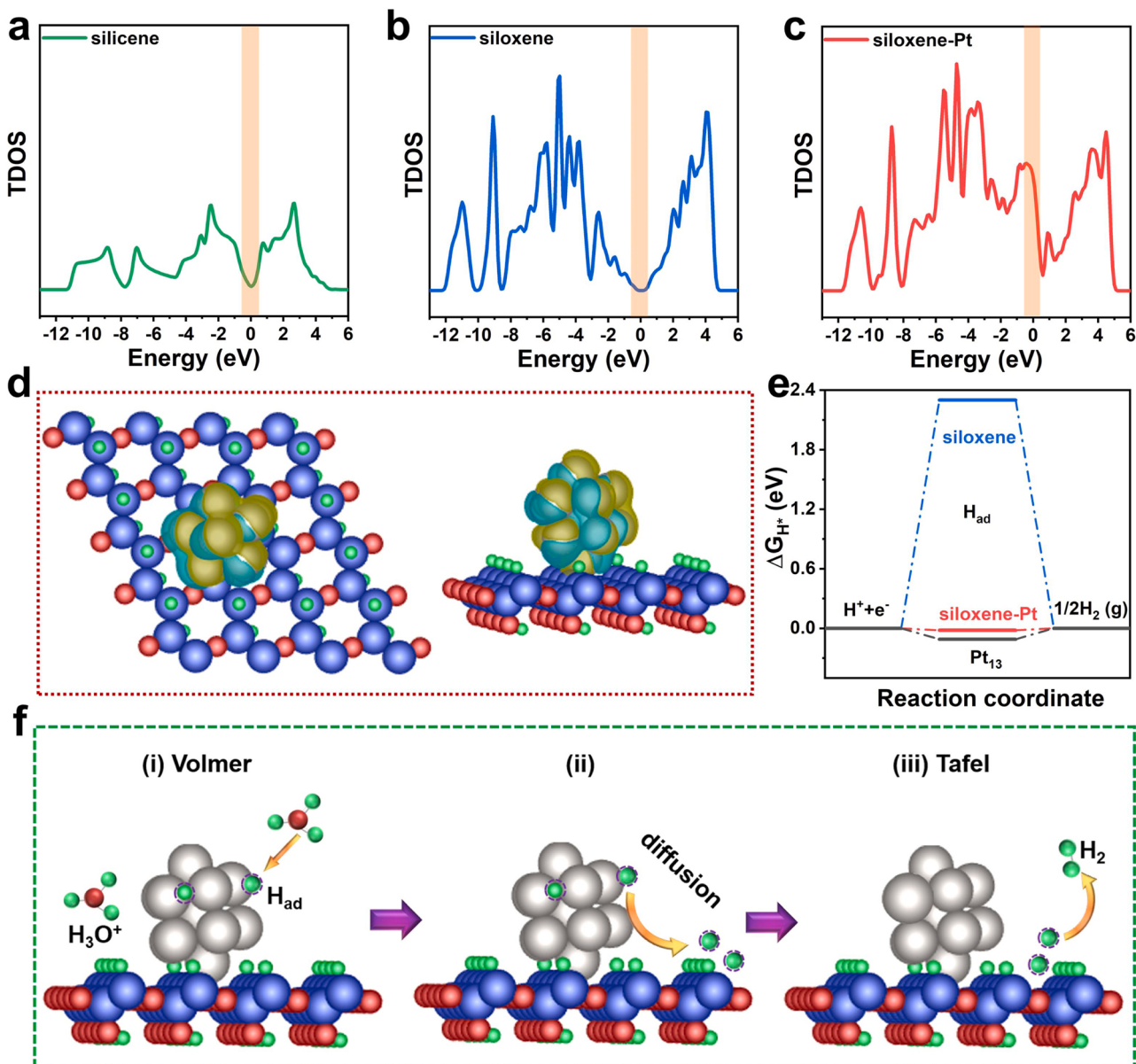


Fig. 6. TDOS images of (a) silicene, (b) siloxene and (c) siloxene-Pt. (d) Differential charge density of Pt_{13} adsorbed on siloxene, the iso-surfaces in yellow and green represent charge repulsion and charge accumulation, respectively. Blue, red, green, and gray balls represent Si, O, H and Pt atoms, respectively. (e) The corresponding calculated standard free energy diagram for HER corresponding to the optimal HER site in siloxene and siloxene-Pt. (f) Schematic representation of the three-step reaction pathway of siloxene-Pt system.

shows three typical models (top view and side view) of pure silicene, pure siloxene and siloxene-Pt, and their corresponding total densities of states (TDOSs) are displayed in Fig. 6a–c. The TDOS of pure siloxene is greatly different from that of pure silicene, demonstrating that the electronic structure of siloxene is significantly affected by abundant functional groups and bridging oxygen. It has been reported that high electron densities near the Fermi level will facilitate H^+ absorption [42], while silicene or siloxene is an indirect-gap semiconductor (Fig. 6a and b). Based on Fig. 6b and c, the DOS near the Fermi level of siloxene-Pt is obviously higher than that of siloxene, indicating that the loading of Pt NPs can effectively change the electron structure of siloxene and thus promote its transition from the Pt metal to siloxene nanosheets, i.e., the siloxene-Pt will be much more conducive to electronic transmission than pure siloxene consistent with the EIS results (Figs. 2i, S5). The DOS analysis is consistent with the XPS result (Figs. 3g, S12), in which the electron interactions at the interfaces between Pt NPs and siloxene substrate triggers the electron redistribution consequently. This is a great advantage of siloxene-Pt featuring especially high carrier mobility and metallicity to offer efficient electrocatalytic performance. Furthermore, the charge density difference in Fig. 6d clearly shows that the loading of Pt NPs has led to the significantly increased internal electron concentration of the system and the promoted charge transfer between Pt NPs and siloxene owing to the strong electron interaction, thereby effectively elevating their carrier mobility and enhancing the electrocatalytic activity. Moreover, the ΔG_{H^*} as a key factor of the HER activity was calculated in Fig. 6e. The optimal value of ΔG_{H^*} of siloxene-Pt is -0.02 eV, extremely close to 0 eV, while a much more positive or negative ΔG_{H^*} will lead to largely reduced HER performance on account of the difficulties in the adsorption or desorption of intermediate H_{ad} , respectively [41,50]. Comparatively, the calculated ΔG_{H^*} of pure siloxene is 2.30 eV, indicating that pure siloxene is inactive for HER. Normally, the electrochemical HER employing metal-support catalysts has been recognized to follow a two-step route: (i) Volmer step, (ii) Heyrovsky or Tafel step. However, in the present case of using siloxene-Pt catalyst, the HER process is believed to feature three steps owing to the strong adsorption of proton on Pt NPs and easy desorption of produced hydrogen from the siloxene support, as shown in Fig. 6f: (i) the H_3O^+ are initially adsorbed on the Pt NPs surfaces to form H_{ad} (Volmer), (ii) the H_{ad} atoms transfer from the surface of Pt NPs to siloxene nanosheets (diffusion), and (iii) the H_{ad} atoms on the siloxene surface integrate with each other to release the H_2 (Tafel). Such a three step route features a much lowered energy barrier (Fig. 6e), in correspondence to the extremely lower Tafel slope of 25.7 mV dec $^{-1}$. The theory calculation results confirm that the HER activity of siloxene-Pt is enhanced dominantly by the electron interactions at the interfaces between Pt NPs and siloxene substrate, i.e., synergistic catalytic effect between the active species and the siloxene substrate.

4. Conclusion

In summary, we have successfully synthesized siloxene nanosheets of abundant surface functional groups via a facile wet-chemistry route, followed by ultralow Pt NPs loading by a photo-reduction approach. The obtained siloxene-p-Pt-2 h exhibits excellent electrocatalytic HER activity, which is far superior to those of silicene-based counterparts, and its corresponding overpotential at 10 mA cm $^{-2}$ and the mass activity are 4 mV lower than and 38 times that of Pt/C, respectively. In addition, the siloxene-p-Pt-2 h-equipment Zn-H₂O fuel cell exhibit an extremely high and stable power density output of 157 mW cm $^{-2}$. Furthermore, a coupled configuration between two Zn-H₂O cells in series and a hydrolyzer has been established for the first time, for the self-powered co-productions of hydrogen from both the fuel cells and electrocatalytic water splitting. The excellent HER performance of siloxene-p-Pt-2 h is attributed to both the homogeneous dispersion of ultra-small Pt NPs (~ 2 nm) enabled by the hydrophilic siloxene substrate possessing abundant surface functional groups and oxygen vacancies, and the

strong electron interaction between the Pt NPs and siloxene substrates which triggers the effective electron transfer between Pt NPs and siloxene substrate for accelerating the adsorption of H^+ and enhancing the electrical conductivity.

CRediT authorship contribution statement

Chang Chen: Conceptualization, Methodology, Validation, Formal analysis, Investigation, Visualization, Writing – original draft. **Han Tian:** Conceptualization, Investigation, Resources. **Zhengqian Fu:** Investigation, Resources. **Xiangzhi Cui:** Conceptualization, Methodology, Supervision, Investigation, Writing – review & editing. **Fantao Kong, Ge Meng, Yafeng Chen, Fenggang Qi and Ziwei Chang:** Investigation, Resources. **Libo Zhu:** Investigation. **Haitao Huang and Bao Yu Xia:** Resources. **Jianlin Shi:** Conceptualization, Methodology, Supervision, Investigation, Writing – review & editing.

Declaration of Competing Interest

The authors declare that they have no known competing financial interests or personal relationships that could have appeared to influence the work reported in this paper.

Acknowledgements

The authors gratefully acknowledge the support of this research by National Natural Science Foundation of China (21835007, 52172110), Key Research Program of Frontier Sciences, Chinese Academy of Sciences (ZDBS-LY-SLH029), the “Scientific and Technical Innovation Action Plan” Hong Kong, Macao and Taiwan Science & Technology Cooperation Project of Shanghai Science and Technology Committee (21520760500), Natural Science Foundation of Shanghai (19ZR1479400), and the State Key Laboratory of Advanced Technology for Materials Synthesis and Processing (Wuhan University of Technology).

Appendix A. Supporting information

Supplementary data associated with this article can be found in the online version at [doi:10.1016/j.apcatb.2021.121008](https://doi.org/10.1016/j.apcatb.2021.121008).

References

- [1] Z.W. Seh, J. Kibsgaard, C.F. Dickens, I. Chorkendorff, J.K. Nørskov, T.F. Jaramillo, Combining theory and experiment in electrocatalysis: Insights into materials design, *Science* 355 (2017) eaad4998, <https://doi.org/10.1126/science.aad4998>.
- [2] P. Cai, Y. Li, G. Wang, Z. Wen, Alkaline-acid Zn-H₂O fuel cell for the simultaneous generation of hydrogen and electricity, *Angew. Chem. Int. Ed.* 57 (2018) 3910–3915, <https://doi.org/10.1002/anie.201712765>.
- [3] C. Wei, S. Sun, D. Mandler, X. Wang, S.Z. Qiao, Z.J. Xu, Approaches for measuring the surface areas of metal oxide electrocatalysts for determining their intrinsic electrocatalytic activity, *Chem. Soc. Rev.* 48 (2019) 2518–2534, <https://doi.org/10.1039/C8CS00848E>.
- [4] P. Zhai, M. Xia, Y. Wu, G. Zhang, J. Gao, B. Zhang, S. Cao, Y. Zhang, Z. Li, Z. Fan, C. Wang, X. Zhang, J.T. Miller, L. Sun, J. Hou, Engineering single-atomic ruthenium catalytic sites on defective nickel-iron layered double hydroxide for overall water splitting, *Nat. Commun.* 12 (2021) 4587, <https://doi.org/10.1038/s41467-021-24828-9>.
- [5] J. Chen, M. Qin, S. Ma, R. Fan, X. Zheng, S. Mao, C. Chen, Y. Wang, Rational construction of Pt/PtTe_x interface with optimal intermediate adsorption energy for efficient hydrogen evolution reaction, *Appl. Catal. B Environ.* 299 (2021), 120640, <https://doi.org/10.1016/j.apcatb.2021.120640>.
- [6] P. Wang, X. Zhang, J. Zhang, S. Wan, S. Guo, G. Lu, J. Yao, X. Huang, Precise tuning in platinum-nickel/nickel sulfide interface nanowires for synergistic hydrogen evolution catalysis, *Nat. Commun.* 8 (2017) 14580, <https://doi.org/10.1038/ncomms14580>.
- [7] J. Zhang, Q. Zhang, X. Feng, Support and interface effects in water-splitting electrocatalysts, *Adv. Mater.* 31 (2019), 1808167, <https://doi.org/10.1002/adma.201808167>.
- [8] Q. Shao, F. Li, Y. Chen, X. Huang, The advanced designs of high-performance platinum-based electrocatalysts: recent progresses and challenges, *Adv. Mater. Interfaces* 5 (2018), 1800486, <https://doi.org/10.1002/admi.201800486>.

[9] Q. Chen, B. Wei, Y. Wei, P. Zhai, W. Liu, X. Gu, Z. Yang, J. Zuo, R. Zhang, Y. Gong, Synergistic effect in ultrafine PtNiP nanowires for highly efficient electrochemical hydrogen evolution in alkaline electrolyte, *Appl. Catal. B Environ.* 301 (2022), 120754, <https://doi.org/10.1016/j.apcatb.2021.120754>.

[10] Y. Chen, R. Ding, J. Li, J. Liu, Highly active atomically dispersed platinum-based electrocatalyst for hydrogen evolution reaction achieved by defect anchoring strategy, *Appl. Catal. B Environ.* 301 (2022), 120830, <https://doi.org/10.1016/j.apcatb.2021.120830>.

[11] X. Huang, J. Tang, T. Qiu, R. Knibbe, Y. Hu, T.U. Schülli, T. Lin, Z. Wang, P. Chen, B. Luo, L. Wang, Nanoconfined topochemical conversion from MXene to ultrathin non-layered TiN nanomesh toward superior electrocatalysts for lithium-sulfur batteries, *Small* 17 (2021), 2101360, <https://doi.org/10.1002/smll.202101360>.

[12] X. Li, Y. Fang, J. Wang, H. Fang, S. Xi, X. Zhao, D. Xu, H. Xu, W. Yu, X. Hai, C. Chen, C. Yao, H.B. Tao, A.G.R. Howe, S.J. Pennycook, B. Liu, J. Lu, C. Su, Ordered clustering of single atomic Te vacancies in atomically thin PtFe2 promotes hydrogen evolution catalysis, *Nat. Commun.* 12 (2021) 2351, <https://doi.org/10.1038/s41467-021-22681-4>.

[13] L. Yi, Y. Ji, P. Shao, J. Chen, J. Li, H. Li, K. Chen, X. Peng, Z. Wen, Scalable synthesis of tungsten disulfide nanosheets for alkali-acid electrocatalytic sulfion recycling and H₂ generation, *Angew. Chem. Int. Ed.* 60 (2021) 21550–21557, <https://doi.org/10.1002/anie.202108992>.

[14] Y. Chen, H. Yao, F. Kong, H. Tian, G. Meng, S. Wang, X. Mao, X. Cui, X. Hou, J. Shi, V₂C MXene synergistically coupling FeNi LDH nanosheets for boosting oxygen evolution reaction, *Appl. Catal. B Environ.* 297 (2021), 120474, <https://doi.org/10.1016/j.apcatb.2021.120474>.

[15] J. Yang, W. Li, D. Wang, Y. Li, Electronic metal–support interaction of single-atom catalysts and applications in electrocatalysis, *Adv. Mater.* 32 (2020), 2003300, <https://doi.org/10.1002/adma.202003300>.

[16] J. Cai, R. Javed, D. Ye, H. Zhao, J. Zhang, Recent progress in noble metal nanocluster and single atom electrocatalysts for the hydrogen evolution reaction, *J. Mater. Chem. A* 8 (2020) 22467–22487, <https://doi.org/10.1039/DOTA06942F>.

[17] M. Ma, J. Xu, H. Wang, X. Zhang, S. Hu, W. Zhou, H. Liu, Multi-interfacial engineering of hierarchical CoNi2S4/WS2/Co9S8 hybrid frameworks for robust all-pH electrocatalytic hydrogen evolution, *Appl. Catal. B Environ.* 297 (2021), 120455, <https://doi.org/10.1016/j.apcatb.2021.120455>.

[18] J. Wan, S.D. Lacey, J. Dai, W. Bao, M.S. Fuhrer, L. Hu, Tuning two-dimensional nanomaterials by intercalation: materials, properties and applications, *Chem. Soc. Rev.* 45 (2016) 6742–6765, <https://doi.org/10.1039/C5CS00758E>.

[19] X. Xu, L. Zhou, D. Ding, Y. Wang, J. Huang, H. He, Z. Ye, Silicene quantum dots confined in few-layer silicene nanosheets for blue-light-emitting diodes, *ACS Appl. Nano Mater.* 3 (2020) 538–546, <https://doi.org/10.1021/acsnano.9b02091>.

[20] K. Krishnamoorthy, P. Pazhamalai, S.-J. Kim, Two-dimensional silicene nanosheets: novel high-performance supercapacitor electrode materials, *Energy Environ. Sci.* 11 (2018) 1595–1602, <https://doi.org/10.1039/C8EE00160J>.

[21] A. Molle, C. Grazianetti, L. Tao, D. Taneja, Md.H. Alam, D. Akinwande, Silicene, silicene derivatives, and their device applications, *Chem. Soc. Rev.* 47 (2018) 6370–6387, <https://doi.org/10.1039/C8CS00338F>.

[22] X. Yan, W. Sun, L. Fan, P.N. Duchesne, W. Wang, C. Kübel, D. Wang, S.G.H. Kumar, Y.F. Li, A. Tavasoli, T.E. Wood, D.L.H. Hung, L. Wan, L. Wang, R. Song, J. Guo, I. Gourevich, A.A. Jelle, J. Lu, R. Li, B.D. Hatton, G.A. Ozin, Nickel@Siloxene catalytic nanosheets for high-performance CO₂ methanation, *Nat. Commun.* 10 (2019) 2608, <https://doi.org/10.1038/s41467-019-10464-x>.

[23] Q. Dai, Q. Meng, C. Du, F. Ding, J. Huang, J. Nie, X. Zhang, J. Chen, Spontaneous deposition of Ir nanoparticles on 2D silicene as a high-performance HER electrocatalyst with ultra-low Ir loading, *Chem. Commun.* 56 (2020) 4824–4827, <https://doi.org/10.1039/D0CC00245C>.

[24] R. Gao, J. Tang, X. Yu, S. Lin, K. Zhang, L. Qin, Layered silicon-based nanosheets as electrode for 4 V high-performance supercapacitor, *Adv. Funct. Mater.* 30 (2020), 2002200, <https://doi.org/10.1002/adfm.202002200>.

[25] W. Zhang, L. Sun, J.M.V. Nsanzimana, X. Wang, Lithiation/delithiation synthesis of few layer silicene nanosheets for rechargeable Li-O₂ batteries, *Adv. Mater.* 30 (2018), 1705523, <https://doi.org/10.1002/adma.201705523>.

[26] J. Zhuang, X. Xu, G. Pelekisis, W. Hao, S.X. Dou, Y. Du, Silicene: a promising anode for lithium-ion batteries, *Adv. Mater.* 29 (2017), 1606716, <https://doi.org/10.1002/adma.201606716>.

[27] S. Li, H. Wang, D. Li, X. Zhang, Y. Wang, J. Xie, J. Wang, Y. Tian, W. Ni, Y. Xie, Silicene nanosheets: a metal-free semiconductor for water splitting, *J. Mater. Chem. A* 4 (2016) 15841–15844, <https://doi.org/10.1039/C6TA07545B>.

[28] Y. Sun, A. Huang, Z. Wang, Transition metal atom (Ti, V, Mn, Fe, and Co) anchored silicene for hydrogen evolution reaction, *RSC Adv.* 9 (2019) 26321–26326, <https://doi.org/10.1039/C9RA04602J>.

[29] J. Liu, Y. Yang, P. Lyu, P. Nachtigall, Y. Xu, Few-layer silicene nanosheets with superior lithium-storage properties, *Adv. Mater.* 30 (2018), 1800838, <https://doi.org/10.1002/adma.201800838>.

[30] S. Wang, T. He, P. Chen, A. Du, K. (Ken) Ostrikov, W. Huang, L. Wang, In situ formation of oxygen vacancies achieving near-complete charge separation in planar BiVO₄ photoanodes, *Adv. Mater.* 32 (2020), 2001385, <https://doi.org/10.1002/adma.202001385>.

[31] K. Xu, L. Ben, H. Li, X. Huang, Silicon-based nanosheets synthesized by a topochemical reaction for use as anodes for lithium ion batteries, *Nano Res.* 8 (2015) 2654–2662, <https://doi.org/10.1007/s12274-015-0772-4>.

[32] T. Okubo, T. Yamada, M. Saito, C. Yodoya, A. Kamei, M. Hirota, T. Takenaka, A. Tasaka, M. Inaba, Carbon coating of Si thin flakes and negative electrode properties in lithium-ion batteries, *Electrochemistry* 80 (2012) 720–724, <https://doi.org/10.5796/electrochemistry.80.720>.

[33] F. Zhang, M. Wang, Z. Wang, K. Han, X. Liu, X. Xu, Nonlinear absorption properties of silicene nanosheets, *Nanotechnology* 29 (2018), 225701, <https://doi.org/10.1088/1361-6528/aa6b8a>.

[34] H. Imagawa, N. Takahashi, T. Nonaka, Y. Kato, K. Nishikawa, H. Itahara, Synthesis of a calcium-bridged siloxene by a solid state reaction for optical and electrochemical properties, *J. Mater. Chem. A* 3 (2015) 9411–9414, <https://doi.org/10.1039/C5TA00321K>.

[35] Y. Luo, L. Tang, U. Khan, Q. Yu, H.-M. Cheng, X. Zou, B. Liu, Morphology and surface chemistry engineering toward pH-universal catalysts for hydrogen evolution at high current density, *Nat. Commun.* 10 (2019) 269, <https://doi.org/10.1038/s41467-018-07792-9>.

[36] H. Qiao, H. Liu, Z. Huang, Q. Ma, S. Luo, J. Li, Y. Liu, J. Zhong, X. Qi, Black phosphorus nanosheets modified with Au nanoparticles as high conductivity and high activity electrocatalyst for oxygen evolution reaction, *Adv. Energy Mater.* 10 (2020), 2002424, <https://doi.org/10.1002/aenm.202002424>.

[37] P. Wei, X. Li, Z. He, Z. Li, X. Zhang, X. Sun, Q. Li, H. Yang, J. Han, Y. Huang, Electron density modulation of MoP by rare earth metal as highly efficient electrocatalysts for pH-universal hydrogen evolution reaction, *Appl. Catal. B Environ.* 299 (2021), 120657, <https://doi.org/10.1016/j.apcatb.2021.120657>.

[38] Z. Liu, K. Wang, Y. Li, S. Yuan, G. Huang, X. Li, N. Li, Activation engineering on metallic 1T-MoS₂ by constructing In-plane heterostructure for efficient hydrogen generation, *Appl. Catal. B Environ.* 300 (2022), 120696, <https://doi.org/10.1016/j.apcatb.2021.120696>.

[39] B. Mohanty, Y. Wei, M. Ghorbani-Asl, A.V. Krasheninnikov, P. Rajput, B.K. Jena, Revealing the defect-dominated oxygen evolution activity of hematene, *J. Mater. Chem. A* 8 (2020) 6709–6716, <https://doi.org/10.1039/DOTA00422G>.

[40] Y. Li, X. Li, H.S. Pillai, J. Lattimer, N. Mohd Adli, S. Karakalos, M. Chen, L. Guo, H. Xu, J. Yang, D. Su, H. Xin, G. Wu, Ternary PtIrNi catalysts for efficient electrochemical ammonia oxidation, *ACS Catal.* 10 (2020) 3945–3957, <https://doi.org/10.1021/acscatal.9b04670>.

[41] J. Yang, B. Chen, X. Liu, W. Liu, Z. Li, J. Dong, W. Chen, W. Yan, T. Yao, X. Duan, Y. Wu, Y. Li, Efficient and robust hydrogen evolution: phosphorus nitride imide nanotubes as supports for anchoring single ruthenium sites, *Angew. Chem. Int. Ed.* 57 (2018) 9495–9500, <https://doi.org/10.1002/anie.201804854>.

[42] S. Ye, F. Luo, Q. Zhang, P. Zhang, T. Xu, Q. Wang, D. He, L. Guo, Y. Zhang, C. He, X. Ouyang, M. Gu, J. Liu, X. Sun, Highly stable single Pt atomic sites anchored on aniline-stacked graphene for hydrogen evolution reaction, *Energy Environ. Sci.* 12 (2019) 1000–1007, <https://doi.org/10.1039/C8EE0288E>.

[43] Z. Ma, H. Tian, G. Meng, L. Peng, Y. Chen, C. Chen, Z. Chang, X. Cui, L. Wang, W. Jiang, J. Shi, Size effects of platinum particles@CNT on HER and ORR performance, *Sci. China Mater.* 63 (2020) 2517–2529, <https://doi.org/10.1007/s40843-020-1449-2>.

[44] M. Sheng, B. Jiang, B. Wu, F. Liao, X. Fan, H. Lin, Y. Li, Y. Lifshitz, S.-T. Lee, M. Shao, Approaching the volcano top: iridium/silicon nanocomposites as efficient electrocatalysts for the hydrogen evolution reaction, *ACS Nano* 13 (2019) 2785–2794, <https://doi.org/10.1021/acsnano.8b07572>.

[45] F. Liao, W. Shen, Y. Sun, Y. Li, H. Shi, M. Shao, Nanospunge Pt modified graphene nanocomposites using silicon monoxides as a reducing agent: high efficient electrocatalysts for hydrogen evolution reaction, *ACS Sustain. Chem. Eng.* 6 (2018) 15238–15244, <https://doi.org/10.1021/acssuschemeng.8b03721>.

[46] W. Shen, B. Wu, F. Liao, B. Jiang, M. Shao, Optimizing the hydrogen evolution reaction by shrinking Pt amount in Pt-Ag/SiNW nanocomposites, *Int. J. Hydrog. Energy* 42 (2017) 15024–15030, <https://doi.org/10.1016/j.ijhydene.2017.03.110>.

[47] Q. Dang, F. Liao, Y. Sun, S. Zhang, H. Huang, W. Shen, Z. Kang, Y. Shi, M. Shao, Rhodium/silicon quantum dot/carbon quantum dot composites as highly efficient electrocatalysts for hydrogen evolution reaction with Pt-like performance, *Electrochim. Acta* 299 (2019) 828–834, <https://doi.org/10.1016/j.electacta.2019.01.031>.

[48] L. Song, T. Zheng, L. Zheng, B. Lu, H. Chen, Q. He, W. Zheng, Y. Hou, J. Lian, Y. Wu, J. Chen, Z. Ye, J. Lu, Cobalt-doped basic iron phosphate as bifunctional electrocatalyst for long-life and high-power-density rechargeable zinc-air batteries, *Appl. Catal. B Environ.* 300 (2022), 120712, <https://doi.org/10.1016/j.apcatb.2021.120712>.

[49] S. Ramakrishnan, D.B. Velusamy, S. Sengodan, G. Nagaraju, D.H. Kim, A.R. Kim, D. J. Yoo, Rational design of multifunctional electrocatalyst: an approach towards efficient overall water splitting and rechargeable flexible solid-state zinc-air battery, *Appl. Catal. B Environ.* 300 (2022), 120752, <https://doi.org/10.1016/j.apcatb.2021.120752>.

[50] X. Zeng, J. Shui, X. Liu, Q. Liu, Y. Li, J. Shang, L. Zheng, R. Yu, Single-atom to single-atom grafting of Pt₁ onto Fe-N₄ center: Pt₁@Fe-N-C multifunctional electrocatalyst with significantly enhanced properties, *Adv. Energy Mater.* 8 (2018), 1701345, <https://doi.org/10.1002/aenm.201701345>.